This article has been accepted for publication in a future issue of this journal, but has not been fully edited. Content may change prior to final publication. Citation information: DOI 10.1109/TIA.2018.2860558, IEEE Transactions on Industry Applications

On the Measurement and Modelling of the Heat Transfer Coefficient of a Hollow-Shaft Rotary Cooling System for a Traction Motor

Y. Gai[1], M. Kimiabeigi[1], Y. C. Chong[2], J. D. Widmer[1], J. Goss[2], U. SanAndres[2], A. Steven[1], D. A. Staton[2]
[1]Affiliation 1; Newcastle University, Newcastle upon Tyne, NE1 7RU, U.K.
[2]Affiliation 2; Motor Design Ltd., Wrexham, LL13 7YT, U.K.

***Abstract*—This paper addresses the heat transfer coefficient (HTC) associated with the hollow-shaft rotor cooling of a traction motor. In such a hollow-shaft cooling system, the coolant is made to flow through the shaft hole in order to cool the rotor. The HTC is estimated using computational fluid dynamics (CFD), where the effect of rotational velocity as well as the coolant flow rate have been accounted for. Experiments are then used to validate the accuracy of CFD models with the assistance of an analytical lumped-parameter thermal network (LPTN) approach. On the basis of CFD simulations and the experimental prototype testing, it is concluded that the rotational speed can significantly increase the convective heat transfer of the shaft hole about 3.8 times at 4500 rpm above the level of the stationary condition. As a result of such analysis, a new dimensionless correlation of the Nusselt number with the Reynolds number is derived.**

***Index Terms*— Cooling, computational fluid dynamics (CFD), heat transfer coefficient (HTC), lumped-parameter thermal network (LPTN), traction motors.**

I. Introduction

In order to be competitive on the market, the design of an electrical traction motor must meet the following essential criteria: a small packaging as well as high torque and high power density. When creating such motors, the designer is inevitably required to consider the problem from a multi-physics perspective. The latter would include looking at electromagnetic, thermal and structural issues in order to meet any particular customer requirements [1, 2]. As regards the thermal analysis, the heat is generated by the electromagnetic losses occurring mainly in the windings and laminations. On the other hand, both the demagnetization of the magnets and the insulation aging may arise due to the temperature increase within the motor.

Having an internal rotor is usually associated with poor heat transfer due to the airgap acting as an insulating material. Poor heat transfer leads to a loss of electromagnetic performance. To improve the cooling, forced air systems with a shaft-mounted fan or an extra blower have been investigated by several authors for totally enclosed fan-cooled (TEFC) motors [3, 4]. A sufficient air flow is created to remove heat from the interior parts of the motor. Alternatively, the motor could be totally flooded and the rotor and stator surfaces directly flushed by a coolant such as water or oil [5]. However, a direct liquid cooling method is not an economical and practical one, due to the extra provisions required for diminishing not only the friction losses, but also the risks of short circuit faults and corrosion. An annular gap or a sleeve between the winding and the airgap is introduced [6, 7] to avoid the friction loss. This ensures the coolant is brought closer to the rotor by providing the minimal thermal resistance between the coolant and the heat source. As an economically viable rotor cooling approach, a hollow-shaft cooling system can be employed in the Tesla S60 induction motor [8]. This mechanism has been explained in a separate tration motor design [9], pointing out that the coolant is introduced into the system via a coupling connected to a stationary inner tube. It is then driven back into the gap between the injection tube and the hollow shaft. Reference [10] alludes to a heat pipe that is inserted through the shaft hole. The heat is dissipated by the metallic plate that is located in the extension of the shaft. The much more detailed rotor cooling systems can be found in [11].

The HTC is a critical parameter essential to the accurate thermal modelling of electrical motors. However, in cases where a hollow-shaft rotor cooling system is employed, heat transfer can be complex. A secondary flow will occur as a result of the shaft rotation. Consequently, due to the centrifugal and Coriolis effect, the cold and dense fluid in the centre will move radially to the wall. As a result, the convective HTC correlations of a stationary case is invalid for a hollow-shaft rotor cooling system. Reference [12] observes that the rotation has a destabilizing effect on a laminar flow, which entail a enhance heat transfer rate. Reference [13] points out that the flow is initially turbulent, whilst the rotation reduces the heat transfer rate due to the stabilizing effect. However, these studies are relevant to cases where a high value in the length to diameter ratio is attained. Reference [14] shows that at the entrance of the pipe, the rotation causes a destabilization on the flow resulting in a swirling. This is due to the large shear caused by the rotating pipe wall. Reference [15] concludes that the pipe rotation entails an increase heat exchange between the moving wall and the air. However, in the literature hitherto there are still limitations in relation to how the unique governing correlations or trends for the liquid coolant convection HTC on a rotating system have been described.

A numerical simulation method may provide reliable estimates regarding the convective HTC of complicated rotary

This article has been accepted for publication in a future issue of this journal, but has not been fully edited. Content may change prior to final publication. Citation information: DOI 10.1109/TIA.2018.2860558, IEEE Transactions on Industry Applications

systems[16]. In [17], the HTC of the air-cooled rotor surface is investigated using the standard k-ε model with the standard near wall treatment. The predicted values derived from the CFD model tend to produce a 30% variation as compared with the experimental results. Different Reynolds-Averaged Navier-Stokes (RANS) turbulence models were used to calculate the HTC of the air-gap for a hydro-generator rotor-stator system [18]. By comparing the HTC results with the experimental data obtained from [19], all turbulence models follow the general trend of the experimental results. The shear stress transport (SST) model, moreover, shows a better agreement with such results.

This paper addresses the hollow-shaft rotor cooling evaluated for use in the 80 kW ferrite magnet traction motor in [20],.as illustrated in Fig. 1, the coolant is forced to pass through a hollow-shaft via two rotary couplings in order to cool the motor. Firstly, the derivations of the convective HTC by CFD are presented. Three RANS improved turbulent models are employed to provide a better understanding of the rotating effect on the flow: 1) A Realizable k-ε model with a two-layer enhanced wall treatment; 2) A SST k-ω model with a non-linear constitutive relation; 3) A Reynolds Stress Transport (RST) model. Secondly, the LPTN model is derived and calibrated by the experimental results to represent the heat transfer of the test rig. As a consequence, the values of internal wall temperature of the shaft T_{iw} and the active heat flux $\dot{q}$, which are both difficult to measure directly, are obtained using the proposed model. Finally, the HTC results have been nondimensionalised into an equation using various dimensionless groups and can be applied in different geometrical contexts with various axial and rotation flow rates.

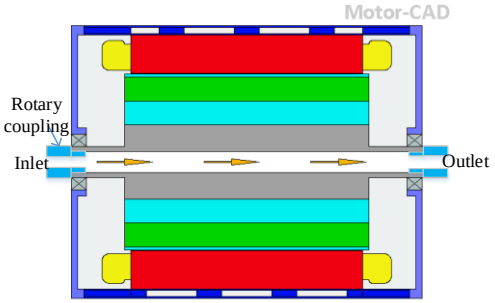

Fig. 1. Hollow-shaft rotor cooling scheme.

II. Test Rig and Measurement

A. Test Rig Setup

Fig. 2 shows the schematic flow diagram of the experimental apparatus, where a circulation system is illustrated. Cool water is supplied to the hollow-shaft by a chiller. A three-way clamp connection T type valve is used to regulate the flow of water in the system and thus the flow rate is measured by a flow meter. The heat transfer test section consists of a horizontal 12 mm internal diameter aluminum tube, with 14 mm thick walls. When assembled, the internal active length is 150 mm. A heater made by resistance wires is connected to the 220 v power supply to transmit the heat to the shaft by air convection, and is installed parallel to the axis of the tube with a 3 mm air gap. Based on the initial testing trials, several measures were taken to minimize the diversion of the heat flow away from the shaft, ensuring most of the generated heat is transferred to the shaft body: a) a polished aluminum cover is wrapped around the heater to enhance the heat reflection back to the shaft; b) a Nano aerogel insulation blanket, with a thermal conductivity of 0.0287 W/mK at 350℃, and with a maximum tolerance of up to 800 ℃ without bursting into flames or suffering any deformation, is packed around the outside of the aluminum cover; c) the shaft and the aforementioned reflective and insulating layers are further placed in a box made from an insulating synthetic stone carbon fiber material.

An electric motor driven by a variable speed drive is used to accelerate the shaft up to 5000 rpm using the pulley. The rotating part of the shaft is connected to the static part with two pipe rotary couplings. On this arrangement, one side can rotate with the shaft, while another side is static to connect with the water pipe. The pipe is further covered with foamed polystyrene in order to minimize the heat transfer to the ambience and to create well-defined boundary conditions.

B. Temperature Measurement

As illustrated in Fig. 3, two four-wire Omega Pt100 sensors (9, 10) with an accuracy of ± 0.05 ℃ are mounted using equal tees to measure the inlet and outlet coolant temperatures. The Pt100 sensor is a type of Resistance Temperature Detector (RTD) that converts the voltage drops of the thermocouples to digital values. RTDs possess the highest stability among temperature transducers and the output is also very linear, thus making RTDs a good choice when highly accurate and long-term measurements are required.

In order to provide an indicator for the thermal model estimation, shaft surface temperature has been monitored. To avoid the complexity associated with rotary part measurements [21], a subminiature noncontact Omega infrared thermometer (A, B) [22] is employed. In practice, due to the partial transmission through the surrounding air, the signal received by the sensor can be attenuated. In addition, the infrared signal might capture the radiation in the environment which is reflected onto the shaft. On these bases, and to improve the radiative heat flux emitted purely by the cylinder, the latter is painted black to achieve a maximal emissivity of 0.94 ± 0.01, as determined by calibration. In addition, a second calibration is taken in respect of the shaft at rest by a K type thermocouple (No. 3, 4).

Three K type thermocouples (No. 6, 7, and 8) are embedded in the Nano aerogel cover to avoid excessive temperature rise in this region. Another K type thermocouple (No. 5) stainless steel probe is attached to the heater to monitor its temperature. The bearing temperature, taken as an indicator to evaluate the thermal model is measured using a K type thermocouple (No. 1, 2).

All the K type thermocouples were calibrated against an Omega surface mount Pt100 element reference with an accuracy of ± 0.07 ℃ by inserting into a Carbolite oven at a range of 20 to 120 ℃. As a result, the errors are maintained within an accuracy margin of ±1 %. The location of the sensor described above ensures exposure to the local heat and temperature distribution in different regions of the testing set-up. This will be examined in the analytical calculations in the following chapters.

This article has been accepted for publication in a future issue of this journal, but has not been fully edited. Content may change prior to final publication. Citation information: DOI 10.1109/TIA.2018.2860558, IEEE Transactions on Industry Applications

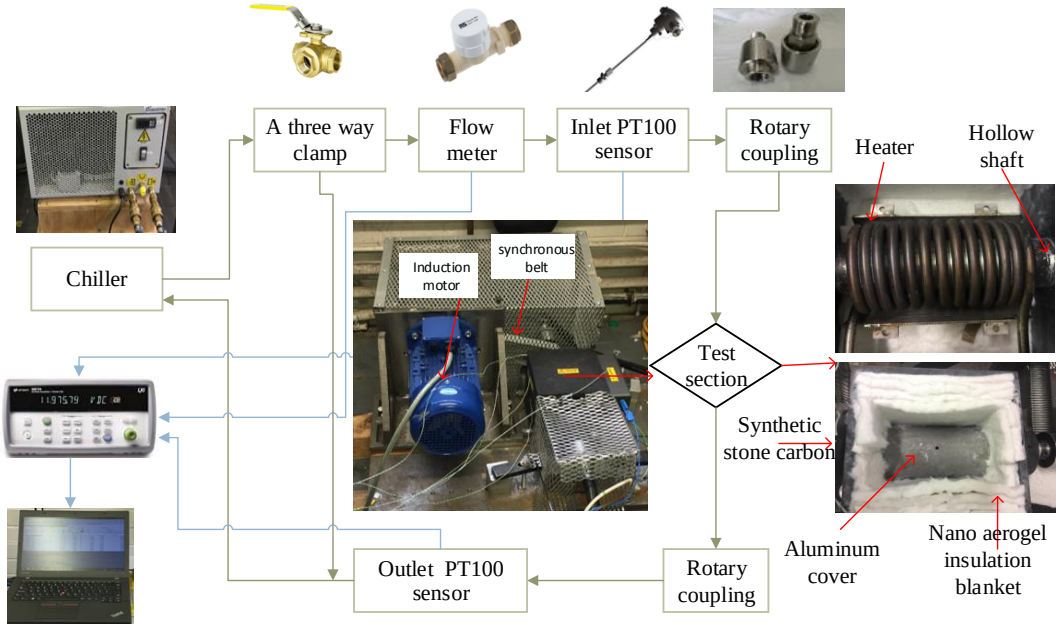

Fig. 2. Experiment setup (blue arrow indicates cooling system loop, orange arrow for the data acquisition system).

All the thermocouples are connected to the Agilent Technologies 34970A which combines data logging and data acquisition features. Through the built-in RS232 interface, the measured data can be sent to a connected computer. Measurements of the test variables are taken at each experimental condition for at least 30 minutes after equilibrium conditions have been established.

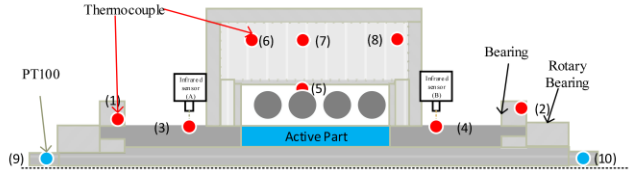

Fig. 3. Temperature sensor locations

C. *Water Flow Rate*

In order to understand the effect of axial flow on the HTC, it is necessary to know the flow rate at which the water passes through the hollow shaft. RS Pro radial flow turbine flow meter is used here and provides a pulsed output proportional to the flow rate. The flow sensor is also connected to the Agilent Technologies 34970A for recording the frequency of the output pulses. The relation of frequency f (pulses per second) vs flow rates Q (litres per minute) is provided in (1), where k is the conversion ratio, which may be different for various coolant viscosities and densities. After calibration, an appropriate k value is 20 in relation to the water.

$$Q = f/\mathrm{k} \tag{1}$$

D. *Control of Heater Unit*

The heater is connected to a variable transformer that is used to adjust the levels of power. The Fluke True RMS Clamp meter is used to measure the voltage (V) and the current (I). The power P_h dissipated from the heater can be calculated from (2).

$$P_h = VI \tag{2}$$

III. Thermal Modelling

The merit of LPTN lies in the fact that the computational cost is less demanding as compared to using any numerical method (e.g. CFD). Once the model parameters are known, the resulting set of thermal algebraic and differential equations which completely describe the thermal performances of the machine at steady and transient states can be computed with ease. On the other hand, for complex fluid motion and convective heat transfer phenomena, the CFD method is used to provide inputs into the LPTN model. The coupled CFD and LPTN are processed as shown in Fig. 4.

The input boundary condition of LPTN model setup for the hollow shaft rotary cooling system is based on test rig. Firstly, the LPTN model setup is calibrated at a stationary case with the HTC from Gnielinski's correlation [23]. By comparing the results between the test and the LPTN models, it can be concluded that the developed LPTN model is able to represent the heat path taken in the test. After that the initial HTC under rotation conditions is investigated using CFD and thus this HTC is the input boundary condition. The output of the LPTN model is the shaft external wall temperature. At this point, a decision is made to carry on or not depending on the outcome of a comparison with the test results. If external wall temperature of the shaft derived from the LPTN model are not the same as those obtained from the experiment, then a new iteration of the HTC is required until the difference of two results obtained between the LPTN model and the experiment converge within a reasonable margin of error (±1 %). After the two sets of measurements more or less match, the next step can be taken in the flow chart, in which the active part of the shaft becomes the focus. A second decision is needed at this

This article has been accepted for publication in a future issue of this journal, but has not been fully edited. Content may change prior to final publication. Citation information: DOI 10.1109/TIA.2018.2860558, IEEE Transactions on Industry Applications

new stage involving a comparison of the HTC as between the active part of the shaft on the one hand and its initial estimation value on the other. If the two sets of the HTC results match, the initial estimation value is the final requirement. Otherwise the LPTN model should be modified by increasing the number of layers and thermal resistance. The flow chart has to restart until the satisfactory results. The proposed CFD and LPTN models respectively will be explained in detail in the following sections.

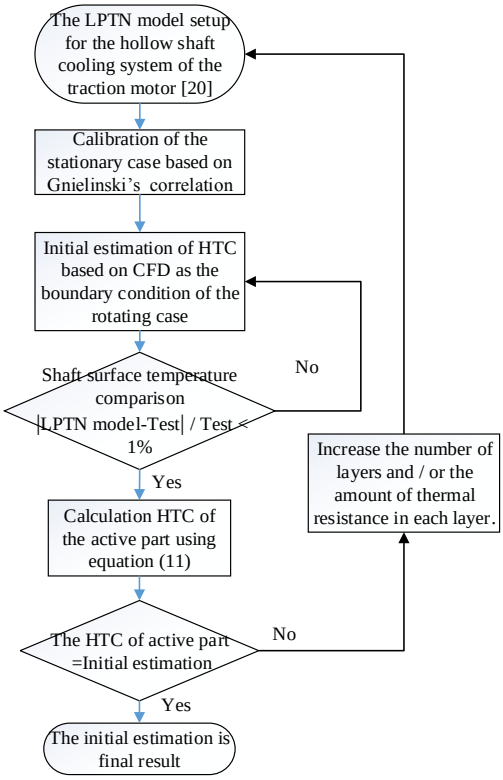

Fig. 4. Flow chart of coupled thermal analysis.

A. CFD

1) The Hollow-Shaft Modelling and Mesh Definition

Instead of a whole machines, only a three dimension of hollow shaft was modelled to simulate flow dynamic and heat transfer in the STAR-CCM+ Version 10.06 [24]. A three dimensional mesh of the hollow shaft is shown in Fig. 5 (a). The active part of the shaft is 150 mm in length with an internal hole (for the passage of coolant) of 12 mm in diameter. Fig. 5 (b) shows a symmetrical cross section of the model. The white region refers to the solid shaft, in relation to which the computational cells need to be calculated using the heat energy equation. Whereas for the fluid regions (as represented by the blue domain), not only the heat equation but also the flow and RANS equations need to be resolved. As for the properties of the coolant and the shaft in the CFD model, pure water and aluminium are used to represent them respectively. The water is assumed to be an incompressible Newtonian fluid with constant fluid properties because the Mach number is far less than 0.3.

Polyhedral mesher is employed to generate a volume mesh that is composed of polyhedral-shaped cells. A conformal mesh is created encompassing separate geometrical parts without interrupting the continuity of the mesh between the solid and the fluid domains. In addition, prism layer mesh is used to add prismatic cell layers next to wall boundaries to capture velocity and thermal boundary layers at the wall. The mesh size is set to be 2 mm and 10 prime layers are used to generate orthogonal prismatic cells next to wall surfaces with ratio of 1.4 for layer stretching. As a result, the total number of computational cells of fluid is approximately 0.15 million, whereas for solid, it is about 0.5 million.

2) Governing Equations and Turbulent Models

In Reynolds averaging, the solution variables in the instantaneous NS equations are decomposed into the time-averaged and fluctuating components. The fluctuations of the flow velocity generated in the momentum equations are known as Reynolds stress tensors that represent the effects of turbulence. The RANS (3-4) and heat energy (5) conservation equations for a steady-state operation are as follows:

$$\frac{\partial U_i}{\partial x_i} = 0 \tag{3}$$

$$\rho \frac{\partial}{\partial x_j}\left(U_i U_j\right) = -\frac{\partial P}{\partial x_i} + \frac{\partial}{\partial x_j}\left(2\mu S_{ij} - \rho\overline{u_i' u_j'}\right) \tag{4}$$

$$\rho C_p U_j \frac{\partial T}{\partial x_j} = \alpha \frac{\partial^2 T}{\partial x_j \partial x_j} \tag{5}$$

Where μ is the fluid dynamic viscosity; ρ is the fluid density; C_p is the specific heat; U, u are the fluid time-averaged and fluctuating velocity component respectively; T is the fluid temperature component; α is the thermal diffusivity; s_{ij} is the mean strain-rate tensor, $-\rho\overline{u_i' u_j'}$ is the symmetric Reynolds stress tensor with six components.

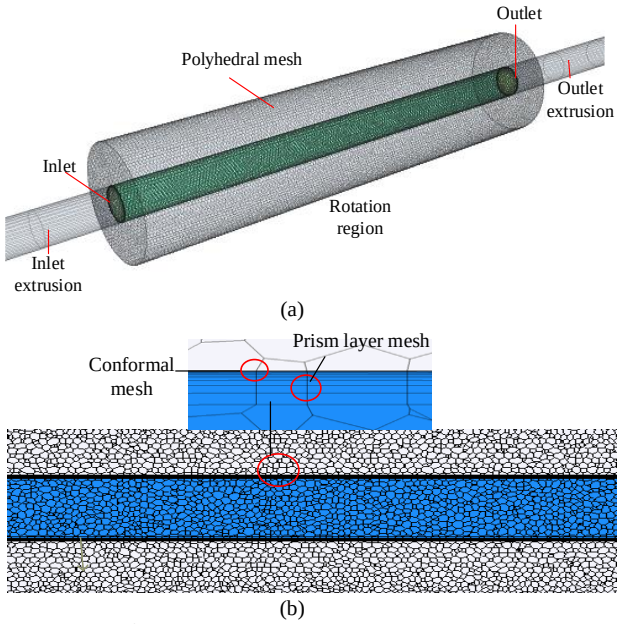

Fig. 5. Mesh setup for the (a) 3-D (b) cross section plane (Grey – Solid, Blue – Liquid) models.

A rotating reference frame is created to model the scenario where, alongside the coolant, the rotation of the shaft for the steady state takes place. A constant rotational force is generated to mimic rotating effects in the rotating domain.

This article has been accepted for publication in a future issue of this journal, but has not been fully edited. Content may change prior to final publication. Citation information: DOI 10.1109/TIA.2018.2860558, IEEE Transactions on Industry Applications

Based on the finding in [14], the rotation may destabilize the flow due to the large shear caused by the rotating pipe wall. The rotational speed of 4500 rpm is sufficient to trigger turbulence at the entrance of the pipe with a rotation Reynolds number of up to 1.5×10^4. Therefore in the present study, turbulent models are employed to provide closure to the RANS equations. The choice of the turbulence model depends on its accuracy concerning the Reynolds stresses and the heat dissipation. Three various turbulence models are selected and compared: 1) A realizable k-ε model with a two-layer enhanced wall treatment [25], which can well capture a flow physics that includes flow separation and rotation at boundary layers [26]. This two-layer approach [27] allows the k-ε model to be employed in the viscous-affected layers by specifying the turbulent dissipation rate and turbulent viscosity as the functions of wall distance. 2) A SST k-ω model [28] includes a non-linear cubic constitutive relation [29]. This relation accounts for the anisotropy of turbulence by adding non-linear functions of the strain and vorticity tensors. 3) A RST model [30], also known as second-moment closure models, is used to directly calculates the components of the specific Reynolds stress tensors by solving their governing transport equations rather than solving the simplistic eddy viscosity equation based on Boussinesq approximations.

3) Boundary Conditions and Wall Treatment

The heat source similar to that of the experiment is applied with a uniform distribution to the shaft surface and can be functionally defined as the heat lost from a machine. The external surface of the shaft is modeled as an adiabatic boundary condition. On this basis, all the heat is dissipated to the coolant through a forced convection between the shaft's internal surface and the fluid. An inlet extrusion region at the inlet boundary is set in order to create a fully turbulent flow. The flow velocity is also set at the top of the inlet extrusion. An extrusion at the flow outlet is also put in place to avoid any flow reverse and, in such a context, 0 pa is defined as any flow that takes place at the top of the outlet extrusion. The inlet temperature and ambient temperature are both fixed at 20℃.

The turbulence models are only valid outside of the viscous-affected region of the fluid boundary layer. This region is close to the solid walls and the flow field is dominated by shear stress due to the wall friction and damping of the turbulent velocity fluctuations perpendicular to the boundary. Hence, an all y+ wall treatment model [31] is applied for the profile of the mean flow quantities in the wall boundary layers. High resolution mesh is created at the wall boundary layer with the wall cell $y+ \leq 0.2$ to achieve accurate predictions in relation to the flow and turbulence parameters.

B. The LPTN Model

A LPTN model of the system is developed using PORTUNUS [32]. To simplify the thermal model, the following assumptions are made:

1) The outer surface of the shaft is modeled as an adiabatic boundary condition.

2) The heat path goes through the shaft via conduction in the axial and radial directions, and via convection from the shaft walls to the coolant fluid. Unlike conduction and convection, radiation is not considered in this paper.

3) The radial and axial heat flows are independent of each other.

4) The heat is transferred to the shaft in a uniform manner and is thus evenly distributed in the body of the shaft.

1) The Equivalent Thermal Network

The number of model components used depends on a balance to be struck between the accuracy of the model on the one hand and its simplicity on the other. The shaft is divided into seven layers consisting of the following: three middle layers representing the active part; two side layers representing the bearings; and two remaining layers as the link function (see Fig. 6). The red and yellow arrows display the heat from the heater and the bearings, the light blue represents the solid conductivity, while the heat that transfers from the shaft to the coolant is indicated by purple arrows. The diagram of a one layer model is shown in Fig. 7, which consists of two major parts: the solid conductive circuit and the fluid convective circuit. The thermal resistances of the shaft are visualized as green blocks. R_{cd_a}, R_{cd_r} which are associated with the axial and radial heat flows respectively. The orange block (R_{cv}) represents the convective heat transfer from the shaft to the coolant. The heat flow in the coolant is modelled as a solid, with the conductive resistance R_{cd_w} displayed as the light blue block. The input temperature (T_{in}) of the flow is the output temperature of the previous layer and this output temperature is measured by the temperature meter (TM_c). The initial flow temperature can be derived from the temperature sensor (No. 9).

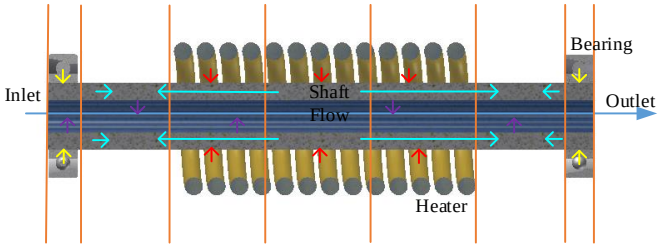

Fig. 6. Representation of the 7 nodal-network layers and heat transfer path.

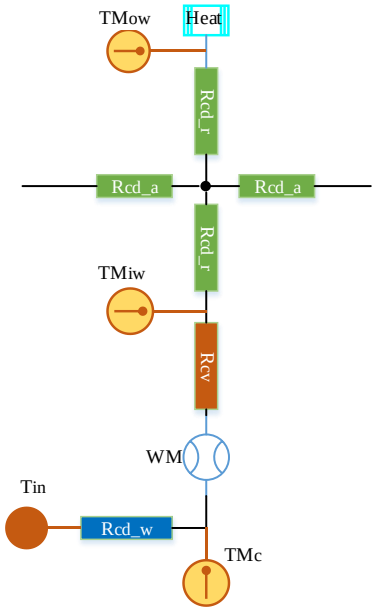

Fig. 7. One layer of developed LPTN model.

This article has been accepted for publication in a future issue of this journal, but has not been fully edited. Content may change prior to final publication. Citation information: DOI 10.1109/TIA.2018.2860558, IEEE Transactions on Industry Applications

In the heat-transfer network, a thermal resistance circuit describes the main paths for the power flow, enabling the temperatures of the various components for a given heat source to be predicted. The thermal-conduction resistances and thermal-convection resistances, except that for the coolant, are defined as (6) and (7). The coolant thermal-conduction resistance is defined as (8). The linear formulations are used to replace the partial differential equations in order to express the thermal state and thus to minimize the computational time.

.

$$R_{cd\_a} = R_{cd\_r} = \frac{l}{\lambda A} \tag{6}$$

$$R_{cv} = \frac{1}{hA} \tag{7}$$

$$R_{cd\_w} = \frac{1}{mc} \tag{8}$$

In (6)-(8), l is the length of heat transfer path; A is the cross-sectional area perpendicular to the path; λ is the thermal conductivity; h is the convective heat transfer coefficient; m is the fluid mass; c is the special heat of the fluid.

2) The Heat Sources

The total heat losses implemented in the model are equal to the heat that is taken away by the coolant. This is because the developed LPTN model is set up as an adiabatic boundary condition at the outer surface of the shaft. Moreover the heat losses transferred to the ambience do not dissipate into the coolant and the influence on the HTC is ignored. When passing through the shaft at a constant flow rate v, the coolant is heated around the shaft's internal wall at a constant temperature, thus raising the temperature of the coolant from T_{in} to T_{out}. Based on the energy conservation equation, the rate of the heat transfer P from the shaft to the coolant is determined by the following equation:

$$P = \rho \cdot v \cdot c_p(T_{out} - T_{in}) \tag{9}$$

3) The Heat Transfer within the Active Part

The Wattmeter (WM in Fig. 7) is placed between the shaft and the coolant and is used to measure the heat transferred from the shaft to the coolant in each layer. From the LPTN model, the active heat transfer P_a can be obtained from (10). The mean convection heat transfer coefficient h of the active part is calculated by (11):

$$P_a = W_1 + W_2 + W_3 \tag{10}$$

$$h = \frac{P_a}{A(T_{iw} - T_{ref})} \tag{11}$$

$$T_{ref} = \frac{T_{ia} + T_{oa}}{2} \tag{12}$$

Where W_1, W_2, W_3 are the values of the Wattmeter in the three layers of the active part; T_{iw} is the average temperature of the shaft's internal wall, which is measured by TM_{iw}. T_{ia}; T_{oa} are the inlet and outlet flow temperatures in the active part, which can be obtained by temperature meter TM_c.

IV. Results and Discussion

In practice, the correlations of the convective HTC (h) have been developed for the water hollow-shaft cooling to show that the Nusselt number Nu mainly depends on the axial Reynolds number Re_a and the rotational Reynolds number Re_r [33]. The tests were carried out with a rotational speed ranging from 0 to 4500 rpm ($0< Re_r <16890$) and a variable flow rate varying from 2 to 6 L/min ($3521< Re_a <10563$). The Prandtl number Pr of water is 7 at inlet temperature of 20 °C. These numbers are defined as:

$$Nu = hd/\lambda \tag{13}$$

$$Re_a = 4Q\rho/\pi\mu d \tag{14}$$

$$Re_r = \omega d^2\rho/2\mu \tag{15}$$

$$Pr = \mu c_P/\lambda \tag{16}$$

A. The Static Testing

In cases where the validation of the experimental method is carried out, the shaft is required to be at rest, so that the dynamic effects due to the rotational speed can be better highlighted. The convective coefficients from the various CFD models and the experiment are compared with the data from Gnielinski's correlations (17) [23], as is depicted in Fig. 8. Suited to the conditions of static testing, [28], Gnielinski's heat transfer correlation is applied to fully developed turbulent flows (i.e.$3000 < Re_a < 5\times 10^6$). At the same time, the Darcy friction factor (f) from the Moody chart is taken into account.

$$Nu = \frac{f}{8}\frac{(Re_a - 1000)Pr}{1 + 12.7\left(\frac{f}{8}\right)^{0.5}(Pr^{\frac{2}{3}} - 1)} \tag{17}$$

Where $f = (0.79\ln(Re_a) - 1.64)^{-2}$.

It is noted here that the three different turbulence models and the experimental data closely follow the trend of Gnielinski's correlation, with the RST and the k-ε models showing the smallest and the largest deviations respectively. These variations can be partly explained due to the rough shaft internal wall surface as compared to the perfectly smooth one assumed in the modeling. In addition, the heat is not evenly radially distributed in the shaft, causing the external wall temperature of the shaft to rise higher than on the internal.

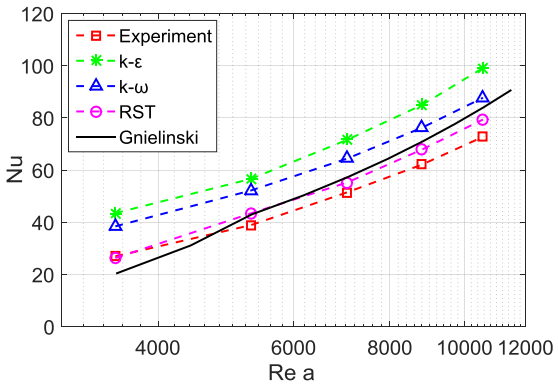

Fig. 8. Evolution of the Nusselt number with the axial Reynolds number.

This article has been accepted for publication in a future issue of this journal, but has not been fully edited. Content may change prior to final publication. Citation information: DOI 10.1109/TIA.2018.2860558, IEEE Transactions on Industry Applications

B. *The Rotating Shaft with an Axial Flow*

Two different steps were taken to calculate the input loss with the heater off and on, respectively, and from (9).

1) Rotating the shaft with the heater off: P_1 is the bearing friction loss as a result of the shaft rotation. Through the experimental results, it is realized that the temperature of the end with the pulley drag is higher than that of the other end, suggesting that the drive end (DE) generates more friction loss than the non-drive end (NDE). From the test and the specification data of the bearing manufacturer [34], a DE to NDE bearing loss ratio of 1.2 is calculated and incorporated in the model.

2) Rotating the shaft with the heater on: P_2 is the losses transferred to the shaft from the heater in addition to the bearing friction losses. Therefore, $(P_2 - P_1)$ is taken as the net loss that the shaft receives from the heater.

Table I lists the measured losses calculated from (9) and active heat transfer from (10) at the axial Reynolds number 4401 with various rotational Reynolds numbers. Due to the short length of the shaft, the dynamic flow losses and windage loss are ignored. The resulting losses are assumed to be evenly transferred to the shaft as the heat source. It can be noticed that all the results obtained in Table I are proportional to the rotating speed. This is because bearing friction losses rise at higher speeds. The input power of the heater is gradually raised by a transformer to highlight the variable performance when the rotating speed is increased. The amount of loss from heater is close to the heater power P_h that is measured by (2). As a result, the active heat transfer increases due to the improvement of heater power and HTC. The net loss between heater loss and active heat transfer is dissipated through other layers of shaft.

TABLE I
THE MEASURED LOSSES AND ACTIVE HEATER TRANSFER at Re_a= 4401.

Re_ω	Bearing Loss P_1 (W)	Heater Loss $(P_2$-$P_1)$ (W)	Active heat transfer P_a (W)
3755	58	205	115
7510	115	353	195
11265	175	492	266
15020	242	630	331
16897	271	710	367

A comparison between, first, the measured results from sensors (1, A, B, 2) and, second, the developed LPTN model is presented in Fig. 9. The difference between the two sets of results is explained by the fact that the thermocouples (No. 1, 2) are mounted on the surface of the bearings. Due to the thermal resistance between the shaft and the bearings, the temperature of the bearings is lower than the shaft surface temperature. The results obtained from the infrared sensors (No. A, B) gave higher temperature values than the predictions derived from the LPTN model. The non-uniform distribution of the heat, which causes the surface heat density, is higher in the external part of the shaft than internally. However, these differences are all within a reasonable margin of error. It can be concluded that the developed LPTN model is able to represent the heat path taken in the test shaft. The internal wall temperatures are calibrated from the LPTN model and then are used to calculate the HTC.

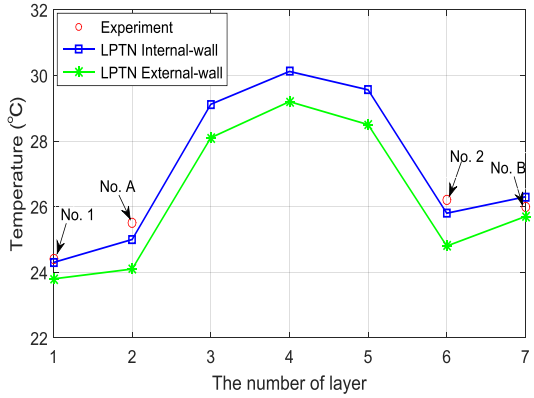

Fig. 9. Comparison of the results between experiment and LPTN model.

A comparison of the results obtained from the different turbulent models is presented in Fig. 10. It is noticed that the value of the HTC increases with the rotational speed in all the methods. To explain the boosting effects two phenomena can be addressed: Firstly, due to the heat source being on the shaft wall surface, the density of the fluid near the walls is less as compared to those close to the center regions. As a result, the centrifugal buoyancy which results from the density variation enhances the temperature exchange between the hot and the cold fluid particles. Secondly, due to the centrifugal and Coriolis effect caused by the shaft rotation, the cold and denser fluid in the center tends to move radially to the wall. This phenomenon changes the flow field in the shaft hole, resulting in a higher convective heat transfer coefficient.

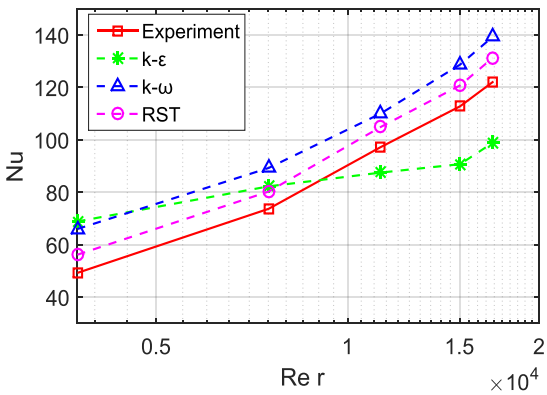

Fig. 10. Evolution of the heat transfer coefficient with different rotational Reynolds numbers for the different models (Re_a= 4401).

Table II presents the relative error $\varepsilon = |Nu_{exp} - Nu_{CFD}|/Nu_{CFD}$ between the three different CFD turbulence models and the experiment. The RST method has a smaller relative error than k-ε and SST k-ω models. The larger discrepancies can be explained by the fact that the k-ε model uses the Boussinesq assumption that the viscous stresses are proportional to the instantaneous rate of the deformation. This makes the Reynolds stresses proportional to the mean rate of deformation of the fluid element with turbulence viscosity assumed to be isotropic. In the case of the SST k-ω model, a non-linear formulation rather than a linear one is used to provide a better agreement with the experimental data. This formulation accounts for the anisotropy by including the non-linear functions of the strain and vorticity-rate tensors, and has

This article has been accepted for publication in a future issue of this journal, but has not been fully edited. Content may change prior to final publication. Citation information: DOI 10.1109/TIA.2018.2860558, IEEE Transactions on Industry Applications

been shown to improve the turbulence predictions in relation to strong secondary flows. However, the simplistic eddy viscosity based on Boussinesq approximations for the Reynolds stresses does not represent the anisotropy of the flow field adequately.

TABLE II
COMPARISON THE RELATIVE ERRORS BETWEEN CFD AND TESTING RESULTS.

Re_a	3521	5281	7042	8802	10563
$\mathcal{E}$_k-ε (%)	28	7	11	24	21
$\mathcal{E}$_k-ω (%)	34	18	13	14	16
$\mathcal{E}$_RST (%)	12	6	7	7	9

To avoid this kind of deficiency of eddy viscosity models, a second order closure scheme RST model has been suggested to directly determine the components of the specific Reynolds stress tensors instead of specifying it by the Boussinesq approximation. Table II shows that the RST model predictions are in good agreement with the data. The RST model has the potential to predict complex flows more accurately than eddy viscosity models because the transport equations for the Reynolds stresses naturally account for the effects of turbulence anisotropy, streamline curvature, swirl rotation and high strain rates. However, the RST model proves very expensive in terms of computational time as five additional equations require some time in order to be solved.

It is found that the RST and SST k-ω models tend to always over-predict the HTC as compared with the experimental measurements. The discrepancy can be explained by the non-uniform distribution of the heat in the shaft surface causing the surface temperature to increase further.

Fig. 11 presents the experimental Nusselt values obtained for the various axial flow rates. The increase in the coolant flow rate enhances the heat transfer between the shaft and the coolant flow. In relation to the imposed flow rate, due to the rotation an increase in the convective heat transfer coefficient can additionally be observed.

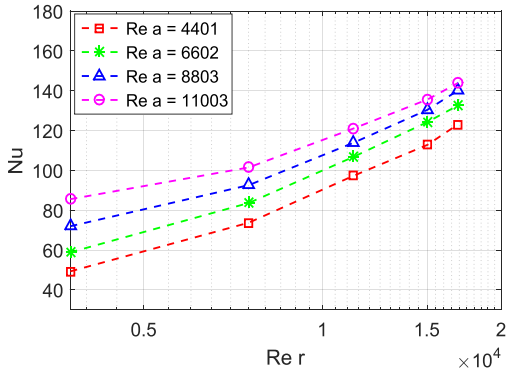

Fig. 11. Evolution of the experimental Nusselt number with $\boldsymbol{Re_r}$ for various axial flow rate.

Based on the experimental results obtained, an equation (18) is proposed to describe the Nusselt number in a steady state based on both the axial and the rotational Reynolds numbers. This is because the convective exchanges on the internal wall of the shaft are determined by the axial and the rotation flow. The exponent of Prandtl number is 0.4 for the heating of the fluid.

$$Nu = ARe_a^B Pr^{0.4} + CRe_r^D Pr^{0.4} \quad (18)$$

From the least square method, with an average relative uncertainly of lower than 10%, and the range of $0< Re_r <16890$ and $3521< Re_a <10563$, the values for A, B, C, D are derived and listed in Table III. This equation can be applied in a number of flow channel geometrical dimensions, as well as at various axial flow rates and rotating speeds. This allows thermal designers to use these parameters to identify the heat transfer coefficients of rotor cooling system with an internal axial flow. As a result, thermal designers can gain an accurate understanding of the thermal model rather than opt for a test trial.

TABLE III
COEFFICIENT FOR CORRELATION

Coefficient	A	B	C	D
Value	7.438E-03	0.09683	9.183E-05	1.358

V. CONCLUSION

In this paper, the HTC of the hollow-shaft rotor cooling for a traction motor is addressed and is applicable in relation to an axial Reynolds number ranging from 3521 to 10563 and a rotational Reynolds number varying between 0 and 16890. Several turbulent flow models are developed in order to give a better understanding of the rotating effect on the flow and to evaluate the convective coefficient. It is concluded that the RST model provides a smaller relative error than the Realizable k-ε and SST k-ω models. The eddy viscosity model based on Boussinesq approximations is less accurate than directly calculating the parameters of the specific Reynolds stress tensors. However, the computational cost of eddy viscosity models is less demanding than a second order closure scheme. The LPTN model is posited to help obtain a number of experimental values that are hard to measure. Through a series of CFD calculations and experiments, it is concluded that the rotational speed of the shaft can significantly enhance the convective HTC of a hollow-shaft cooling system. At the axial Reynolds number 4401, the h for the rotational Reynolds number 16897 is about 3.8 times the h as compared with the stationary case. This is explained by the rotation which generates a destabilizing effect due to the increase in the shear stresses (caused by the wall rotation). As a result, heat exchanges are thus promoted.

The experimental findings have been summarized in a simple equation. The results are presented in the non-dimensional Reynolds and Nusselt numbers respectively, which can be applied in different geometrical contexts with various axial flow rates and rotating speeds. This can provide the opportunity to optimize the thermal design of machines at an early stage without the need for extensive and costly experimentation.

VI. References

[1] N. Uzhegov, E. Kurvinen, J. Nerg, J. Pyrhönen, J. T. Sopanen, and S. Shirinskii, "Multidisciplinary Design Process of a 6-Slot 2-Pole High-Speed Permanent-Magnet Synchronous Machine," *IEEE Transactions on Industrial Electronics*, vol. 63, pp. 784-795, 2016.

[2] S. Ruoho, J. Kolehmainen, J. Ikaheimo, and A. Arkkio, "Interdependence of Demagnetization, Loading, and Temperature Rise in a Permanent-Magnet Synchronous Motor," *IEEE Transactions on Magnetics*, vol. 46, pp. 949-953, 2010.

[3] S. Mizuno, S. Noda, M. Matsushita, T. Koyama, and S. Shiraishi, "Development of a Totally Enclosed Fan-Cooled Traction Motor," *IEEE Transactions on Industry Applications*, vol. 49, pp. 1508-1514, 2013.

[4] W. A. Herbert, "Totally Enclosed Fan-Cooled Squirrel-Cage Induction Motor Options," *IEEE Transactions on Industry Applications*, vol. 50, pp. 1590-1598, 2014.

[5] P. Ponomarev, M. Polikarpova, and J. Pyrhönen, "Thermal modeling of directly-oil-cooled permanent magnet synchronous machine," in *2012 XXth International Conference on Electrical Machines (ICEM)*, 2012, pp. 1882-1887.

[6] A. Tüysüz, F. Meyer, M. Steichen, C. Zwyssig, and J. W. Kolar, "Advanced Cooling Methods for High-Speed Electrical Machines," *IEEE Transactions on Industry Applications*, vol. 53, pp. 2077-2087, 2017.

[7] A. La Rocca, "Thermal analysis of a high speed electrical machine," Ph.D. dissertation, Dept. Elect. Eng., Nottingham Univ., Nottingham,UK, 2016.

[8] M. Popescu, D. A. Staton, A. Boglietti, A. Cavagnino, D. Hawkins, and J. Goss, "Modern Heat Extraction Systems for Power Traction Machines-A Review," *IEEE Transactions on Industry Applications*, vol. 52, pp. 2167-2175, 2016.

[9] A. M. El-Refaie, J. P. Alexander, S. Galioto, P. B. Reddy, K. K. Huh, P. d. Bock, *et al.*, "Advanced High-Power-Density Interior Permanent Magnet Motor for Traction Applications," *IEEE Transactions on Industry Applications*, vol. 50, pp. 3235-3248, 2014.

[10] L. Fedoseyev and E. M. Pearce, "Rotor Assembly with Heat Pipe Cooling System," U.S. Patent 20140368064 A1, Dec. 18, 2014.

[11] Y. Gai, M. Kimiabeigi, Y. C. Chong, J. Widmer, X. Deng, M. Popescu, *et al.*, "Cooling of Automotive Traction Motors: Schemes, Examples and Computation Methods - A Review," in *IEEE Transactions on Industrial Electronics*, ed: to be published. DOI: 10.1109/TIE.2018.2835397.

[12] G. Reich, B. Weigand, and H. Beer, "Fluid flow and heat transfer in an axially rotating pipe-II. Effect of rotation on laminar pipe flow," *Heat and Mass Transfer*, vol. 32, pp. 563-574, 1989.

[13] G. Reich and H. Beer, "Fluid flow and heat transfer in an axially rotating pipe—I. Effect of rotation on turbulent pipe flow," *International Journal of Heat and Mass Transfer*, vol. 32, pp. 551-562, 1989.

[14] K. Kikuyama, M. Murakami, and K. Nishibori, "Development of Three-Dimensional Turbulent Boundary Layer in an Axially Rotating Pipe," *Journal of Fluids Engineering*, vol. 105, pp. 154-160, 1983.

[15] S. Seghir-Ouali, D. Saury, S. Harmand, O. Phillipart, and D. Laloy, "Convective heat transfer inside a rotating cylinder with an axial air flow," *International Journal of Thermal Sciences*, vol. 45, pp. 1166-1178, 2006.

[16] Y. Gai, M. Kimiabeigi, J. D. Widmer, Y. C. Chong, J. Goss, U. SanAndres, *et al.*, "Shaft cooling and the influence on the electromagnetic performance of traction motors," in *2017 IEEE International Electric Machines and Drives Conference (IEMDC)*, 2017, pp. 1-6.

[17] S. J. Pickering, D. Lampard, and M. Shanel, "Modelling ventilation and cooling of the rotors of salient pole machines," in *2001 IEEE InternationalElectric Machines and Drives Conference (IEMDC)* 2001, pp. 806-808.

[18] D. D. Dang, X. T. Pham, P. Labbe, F. Torriano, J. F. Morissette, and C. Hudon, "CFD analysis of turbulent convective heat transfer in a hydro-generator rotor-stator system," *Applied Thermal Engineering*, vol. 130, pp. 17-28, 2018.

[19] N. J. Carew, "Experimental determination of heat transfer co-efficients of salient pole rotors," in *IEE Colloquium on Thermal Aspects of Machines*, 1992, pp. 1-8.

[20] M. Kimiabeigi, J. D. Widmer, R. Long, Y. Gao, J. Goss, R. Martin, *et al.*, "High-Performance Low-Cost Electric Motor for Electric Vehicles Using Ferrite Magnets," *IEEE Transactions on Industrial Electronics*, vol. 63, pp. 113-122, 2016.

[21] C. Jungreuthmayer, T. Bauml, O. Winter, M. Ganchev, H. Kapeller, A. Haumer, *et al.*, "A Detailed Heat and Fluid Flow Analysis of an Internal Permanent Magnet Synchronous Machine by Means of Computational Fluid Dynamics," *IEEE Transactions on Industrial Electronics*, vol. 59, pp. 4568-4578, 2012.

[22] Z. Huang, J. Fang, X. Liu, and B. Han, "Loss Calculation and Thermal Analysis of Rotors Supported by Active Magnetic Bearings for High-Speed Permanent-Magnet Electrical Machines," *IEEE Transactions on Industrial Electronics*, vol. 63, pp. 2027-2035, 2016.

[23] G. Volker, "New Equations for Heat and Mass Transfer in Turbulent Pipe and Channel Flow," *NASA STI/Recon Technical Report* vol. 41, pp. 8-16, 1976.

[24] [Online]. Available: https://mdx.plm.automation.siemens.com/star-ccm-plus.

[25] W. Rodi, "Experience with two-layer models combining the k-epsilon model with a one-equation model near the wall," in *29th Aerospace Sciences Meeting*, ed: American Institute of Aeronautics and Astronautics, 1991.

[26] T.-H. Shih, W. W. Liou, A. Shabbir, Z. Yang, and J. Zhu, "A New K-epsilon Eddy Viscosity Model for High Reynolds Number Turbulent Flows: Model Development and Validation," NASA Lewis Research Center, Cleveland, OH, United States 1994.

[27] M. Wolfshtein, "The velocity and temperature distribution in one-dimensional flow with turbulence augmentation and pressure gradient," *International Journal of Heat and Mass Transfer*, vol. 12, pp. 301-318, 1969.

[28] F. R. Menter, "Two-equation eddy-viscosity turbulence models for engineering applications," *AIAA Journal*, vol. 32, pp. 1598-1605, 1994.

[29] S. Wallin and A. V. Johansson, "An explicit algebraic Reynolds stress model for incompressible and compressible turbulent flows," *Journal of Fluid Mechanics*, vol. 403, pp. 89-132, 2000.

[30] S. Sarkar and B. Lakshmanan, "Application of a Reynolds stress turbulence model to the compressible shear layer," *AIAA Journal*, vol. 29, pp. 743-749, 1991.

[31] "User Guide STAR-CCM + Version 10.06," CD-adapco, Melville, NY, USA, 2015.

[32] Y. C. Chong, D. Staton, I. Egaña, I. R. d. Argandoña, and A. Egea, "Thermal design of a magnet-free axial-flux switch reluctance motor for automotive applications," in *2016 Eleventh International Conference on Ecological Vehicles and Renewable Energies (EVER)*, 2016, pp. 1-8.

[33] D. A. Staton and A. Cavagnino, "Convection Heat Transfer and Flow Calculations Suitable for Electric Machines Thermal Models," *IEEE Transactions on Industrial Electronics*, vol. 55, pp. 3509-3516, 2008.

[34] *[Online]. Available: http://www.skf.com/uk/products/bearings-units-housings/principles/bearing-selection-process/operating-temperature-and-speed/friction-powerloss-startingtorque/index.html*.